ACS APPLIED ELECTRONIC MATERIALS

pubs.acs.org/acsaelm Article

Electronic and Chemical Properties of Nickel Oxide Thin Films and the Intrinsic Defects Compensation Mechanism

Raphaël Poulain, Gunnar Lumbeeck, Jonas Hunka, Joris Proost, Henri Savolainen, Hosni Idrissi, Dominique Schryvers, Nicolas Gauquelin, and Andreas Klein*

Cite This: *ACS Appl. Electron. Mater.* 2022, 4, 2718−2728 **Read Online**

ABSTRACT: Although largely studied, contradictory results on nickel oxide (NiO) properties can be found in the literature. We herein propose a comprehensive study that aims at leveling contradictions related to NiO materials with a focus on its conductivity, surface properties, and the intrinsic charge defects compensation mechanism with regards to the conditions preparation. The experiments were performed by in situ photoelectron spectroscopy, electron energy loss spectroscopy, and optical as well as electrical measurements on polycrystalline NiO thin films prepared under various preparation conditions by reactive sputtering. The results show that surface and bulk properties were strongly related to the deposition temperature with in particular the observation of Fermi level pinning, high work function, and unstable oxygen-rich grain boundaries for the thin films produced at room temperature but not at high temperature (>200 °C). Finally, this study provides substantial information about surface and bulk NiO properties enabling to unveil the origin of the high electrical conductivity of room temperature NiO thin films and also for supporting a general electronic charge compensation mechanism of intrinsic defects according to the deposition temperature.

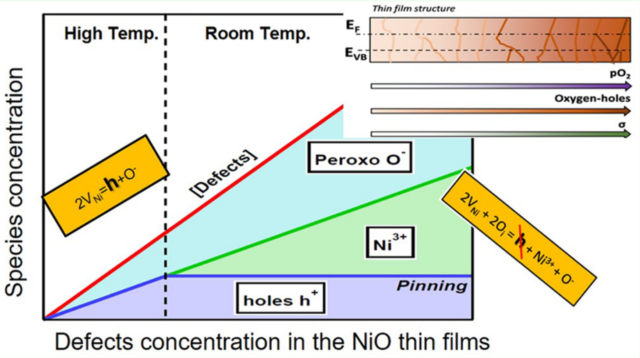

KEYWORDS: *nickel oxide, defects compensation, conductivity, grain boundaries, Fermi level, photoelectron spectroscopy*

INTRODUCTION

Nickel oxide (NiO) is a versatile prototypal charge transfer p-type transition metal oxide material, having a wide optical band gap (∼3.6−4.3 eV) and crystallizing in a cubic rock-salt-like structure.[1,2] An abundant literature describing NiO properties is available because of its potential for being implemented in a wide set of applications, e.g., organic/inorganic electronic devices,[3−9] volatile memory,[10,11] gas sensor,[12] catalysis,[13−16] and energy storage.[15,17−19]

However, the studies are often concentrated on a limited range of conditions and some results can be a priori contradictory.

For instance, it has been reported that high-temperature (HT-)NiO thin films can provide an electrical resistivity and an electrical activation energy (E_A) of 10^7−10^{13} Ω cm[1,2,20] and 0.6 eV, respectively. In comparison, those values fall to 0.1−1 Ω cm[21−23] and 0−0.15 eV[24,25] for room temperature (RT-)NiO thin films. Similarly, the work function values can vary on an energy span of more than 2 eV depending on the preparation temperature.[6,26] Also, it is generally accepted that charge compensation of nickel vacancies V_{Ni}'' is the main driving mechanism leading to p-conductivity in NiO,[3,27−30] while the nature of the electronic compensation can be elusive with the formation of free holes or localized charges either on the oxygen or on the nickel atoms.[22,30]

To complement the understanding of NiO materials properties, we gathered results obtained by in situ photoelectron spectroscopy (PES), scanning transmission electron microscopy coupled with electron energy loss spectroscopy (STEM-EELS), automated crystal orientation mapping (ACOM), ultraviolet−visible spectroscopy (UV−vis) measurements, in situ electrical conductivity, and temperature-dependent electrical conductivity measurements of numerous NiO thin films prepared by reactive sputtering under different temperatures and oxygen concentrations. The results include experiments obtained with NiO thin films deposited on oriented platinum surfaces, silicon, fused silica, fluorine-doped tin oxide, and gold substrates. In this study, we did not find any influence of neither the nature of the substrate nor the orientation of the thin film, which gives a more general

Received: February 20, 2022
Accepted: May 24, 2022
Published: June 7, 2022

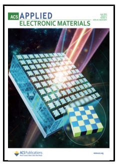

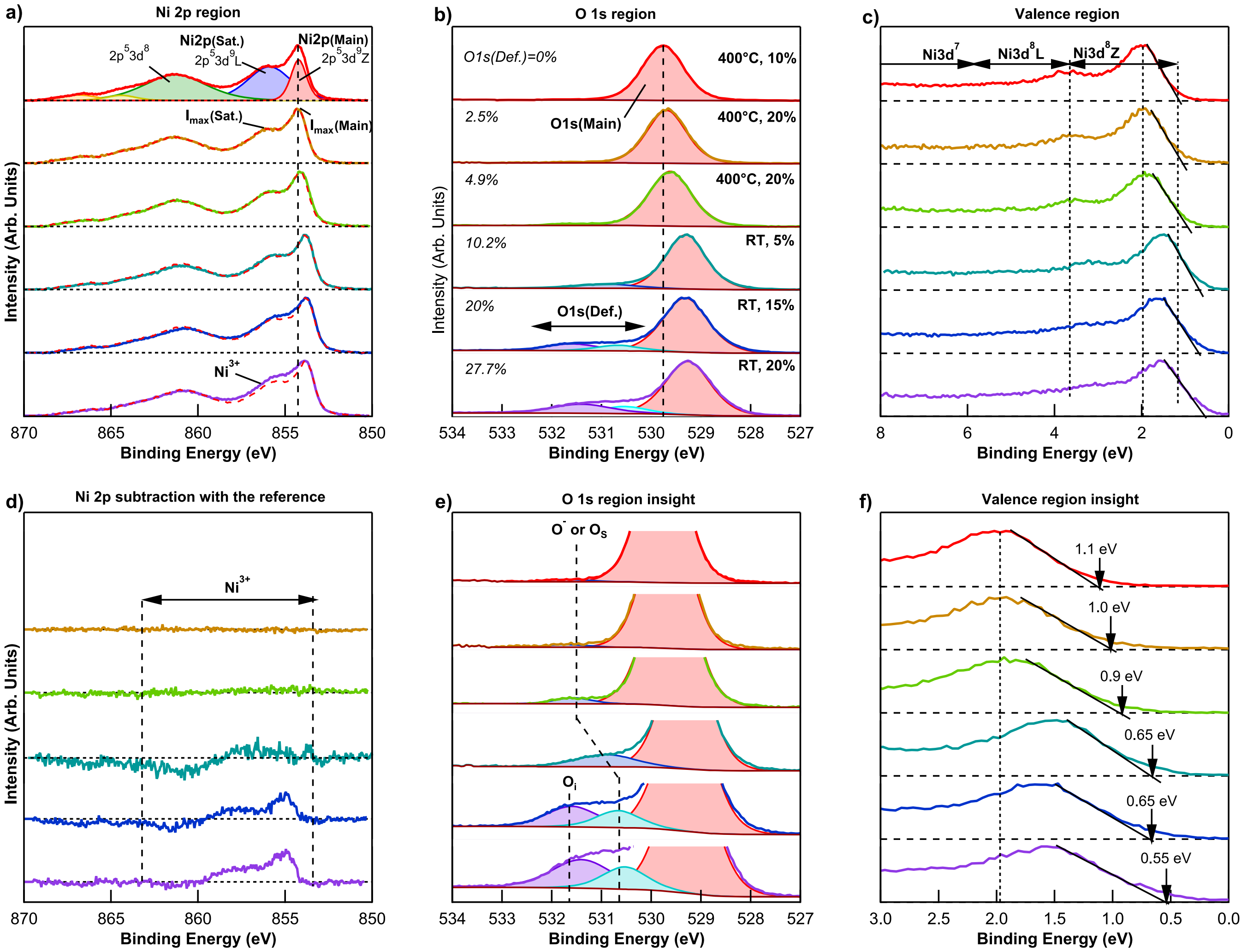

Figure 1. Top row: (a) Shirley background subtracted Ni 2p, (b) O 1s, and (c) valence spectra measured by in situ X-ray PES. Bottom row: (d) residual intensity with the top spectrum from (a), (e) magnified view into the O 1s region, and (f) magnified view of the valence band edge. The patterns are sorted out with increasing O 1s(Def.) weight (%) in the O 1s photoemission. It is worth noting that the two bottom spectra are measured on samples prepared in identical conditions while the results are different. This could originate from unnoticed fluctuation, e.g., in pressure, in the target to substrate distance or in the target aging.

character to our findings. Therefore, for simplification, they are not indicated in this article. It is however worth mentioning that specific surface properties of oriented NiO thin films have been published in two previous studies.[16,31] Finally, we demonstrate that HT- and RT-NiO thin films prepared by reactive sputtering must be distinguished electronically and chemically from each other. RT-NiO thin films are characterized by Fermi level pinning, oxygen-rich grain boundaries, and radically different surface chemistry in comparison to HT-NiO thin films (>200 °C). The resulting analysis opened the possibility to propose an origin to the high conductivity of RT-NiO thin films and also a unifying charge compensation mechanism in NiO thin films according to the preparation temperature.

■ EXPERIMENTAL SECTION

See the Supporting Information section S1 for more details on the sample preparation and the measurement methods.

■ RESULTS

NiO Thin Films Microstructure. The microstructure of the thin films prepared at RT on fused silica and oxide-free silicon substrates has been evaluated by ACOM, and the results are displayed in Supporting Information section 2.1 for convenience. The NiO thin films display grain boundaries with a columnar structure at the microscale. These patterns are observed for RT-NiO thin films deposited on both fused silica and oxide-free silicon substrates, and it is preserved upon thermal annealing of the RT-NiO thin films. The grain boundaries are typically formed during the thin film growth when the substrate does not offer a surface which matches the crystallographic structure of the deposited thin film. It is worth noting that a NiO thin film grown on a lattice matching MgO substrate does not show any grain boundaries (see Figure S5). Such samples could not be studied by photoelectron spectroscopy as they were not conductive enough for transporting charges to the surface, but ex situ electrical measurements are available in Figure S6.

Surface Analysis by Photoelectron Spectroscopy. Typical Ni 2p, O 1s, and valence spectra taken on the NiO

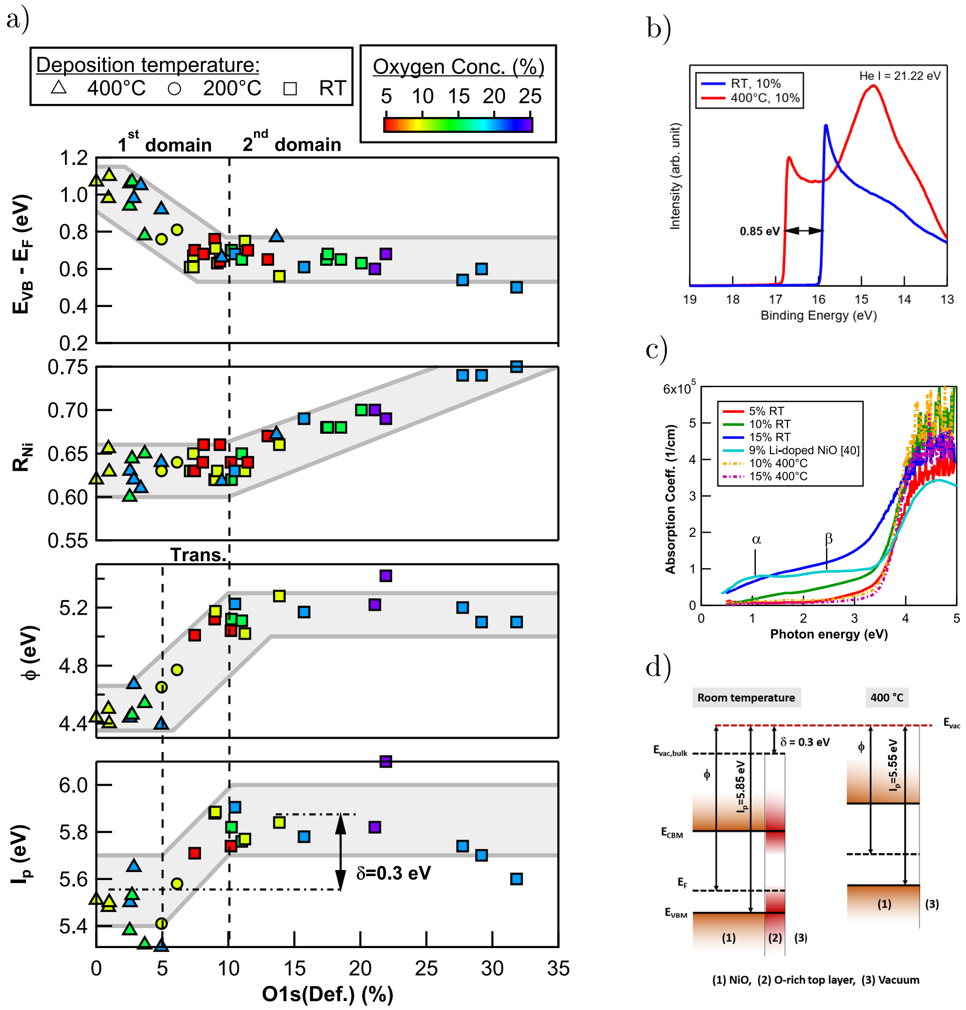

Figure 2. (a) From top to bottom: valence band maximum position to the Fermi level ($E_{VBM} - E_F$), relative peak intensity R_{Ni} (see eq 1), work function (ϕ), and ionization potential ($I_p = E_{VBM} + \phi$) as a function of the weight of O 1s(Def.) in the O 1s region (see Figure 1b). (b) Secondary electron cutoffs measured by in situ ultraviolet PES for samples prepared at room temperature and at high temperature (400 °C) with 10% of oxygen in the sputtering chamber. ϕ is determined from the photon source energy ($h\nu$ = 21.22 eV) distance to the secondary electron cutoff.[42] (c) Optical adsorption for differently prepared NiO thin films. (d) Energy diagram representation of RT- and HT-NiO thin films where E_{vac} and E_{CBM} are the vacuum level and the conduction band minimum, respectively.

thin films by in situ X-ray PES measurements are displayed in Figure 1 according to the weight of the defect state (O 1s(Def.)) to the left of the main O 1s photoemission line (O 1s(Main)). Figure 1 shows only a representative subset of the overall recorded data. Relevant parameters to this study have been extracted from the full data set of measurement and displayed in Figure 2a.

O 1s(Main) is associated with lattice oxygen atoms and the shoulder O 1s(Def.) to defects in the NiO thin film structure as it is prominent in a deposition environment favoring their formation, i.e., at RT and high oxygen concentration (20–25%) while it can be suppressed at high temperature (400 °C) and low oxygen concentration (∼10%).

The O 1s(Def.) shoulder can be associated with oxygen related species formed in or on the NiO thin films. The formation of a hydroxide layer on the NiO thin films due to the surface reaction with remaining water molecules in the UHV chamber is not considered as this would shift the Fermi level upward and the work function downward,[31] which is not observed with the accumulation of the species in the O 1s(Def.) region as shown in Figure 2a. Also in Figure 1e, the deconvolution of this shoulder for the thin films produced at RT and high oxygen concentration shows two electronic states in contrast to the thin films produced at HT or at low oxygen concentration. We finally assumed that the lowest and the highest binding energy components of the O 1s(Def.) feature can be associated with peroxo species (O^-) which are typically found in transition metal compounds[32] or surface oxygen (O_S) which could stabilize the NiO thin films[31] and, with regards to the results discussed in this study, oxygen interstitial (O^{2-}), respectively.

The Ni 2p region is the result of numerous photoemission lines, typical of the NiO charge transfer nature and the strong hybridization of the nickel−oxygen orbitals.[33−37] Following the work of Taguchi et al.,[37] photoemission from the Ni 2p orbital can result in three different final states: the Ni $2p^5 3d^8$, the Ni $2p^5 3d^9 \underline{L}$, and the Ni $2p^5 3d^9 \underline{Z}$ states (top spectra in Figure 1a). $\underline{Z}$ and $\underline{L}$ indicate that the resulting holes from electrons photoemission are located either in a Ni 3d orbital or after a charge transfer in a O 2p orbital (the ligand), respectively.[38] Two minor electronic states are evidenced in the 864−970 eV region, but their nature has not been identified. For

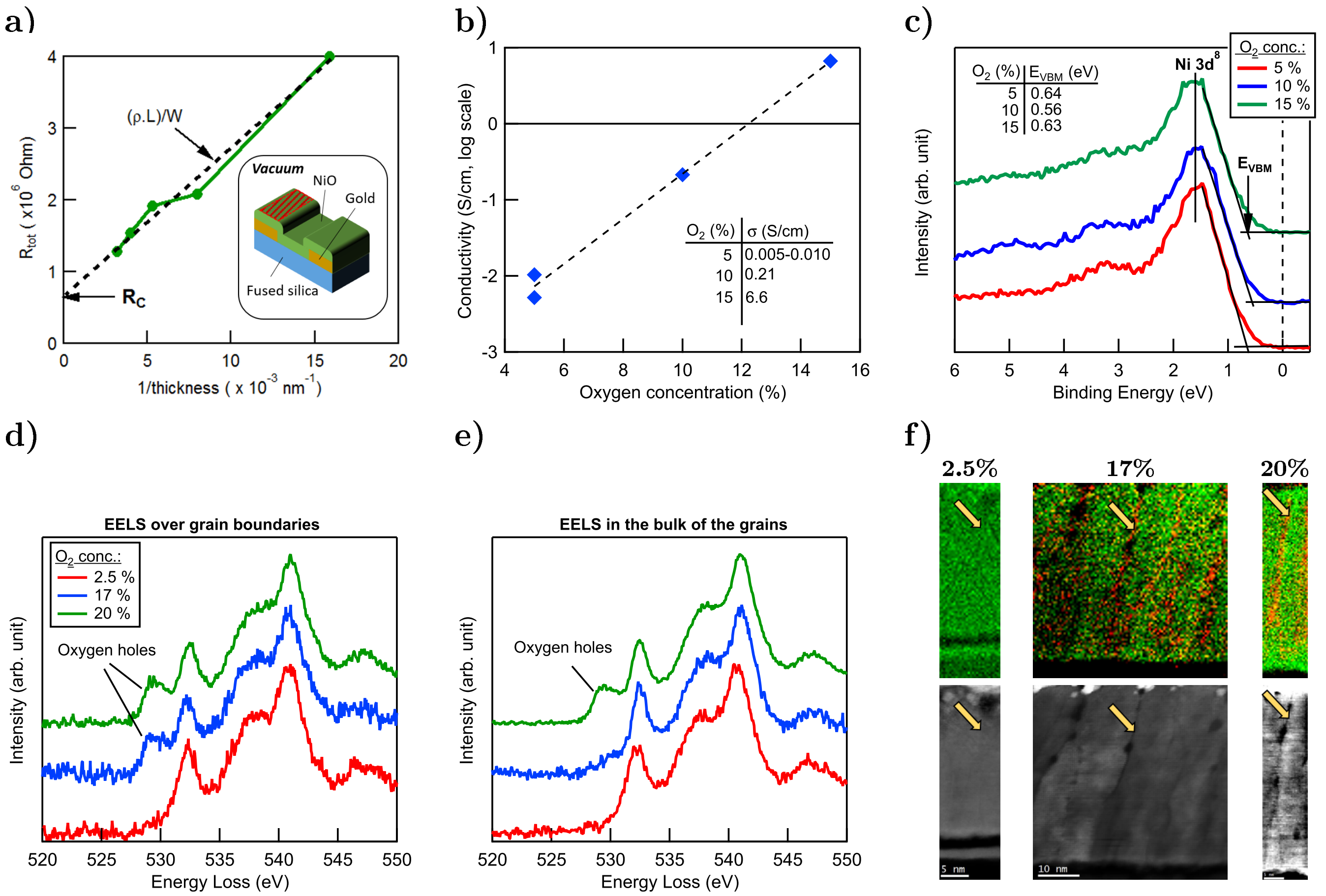

Figure 3. (a) In situ conductivity measurement setup, (b) in situ conductivity of RT-NiO thin films according to the oxygen concentration, and (c) in situ photoemission measurements of the valence band regions realized after the in situ electrical measurements. (d) EELS obtained on grain boundaries and (e) in the bulk of the grains for three RT-NiO thin films deposited on oxide free silicon and (f) contrasted bicolor images (top row) based on the prepeak associated with oxygen holes for which the reddest, the more concentrated, and corresponding annular dark-field images (bottom row) where grain boundaries are highlighted with yellow arrows.

simplification, for the rest of the study, the Ni 2p^{5}3d$^9\underline{L}$ and the Ni 2p^{5}3d$^9\underline{Z}$ orbitals will be termed the satellite peak Ni 2p(Sat.) and the main peak Ni 2p(Main), respectively (see Figure 1c). At this level, the Ni 2p (Sat.) cannot be directly associated with the presence of Ni^{3+}. However, in Figure 1d, the difference of the spectra with the reference Ni 2p spectra highlights the buildup of an extra electronic state in the Ni 2p(Sat.) region (855−860 eV) with increasing O 1s(def.) weight. To evaluate the Ni 2p distortion, the photoemission intensities of the Ni 2p(Main) and the Ni 2p(Sat.) lines are compared:

$$R_{\mathrm{Ni}} = \frac{I_{\max}(\mathrm{Sat.})}{I_{\max}(\mathrm{Main})} \tag{1}$$

where $I_{\max}$ is the maximum in intensity of the corresponding peak (see second spectra in Figure 1a) and R_{Ni} the intensity ratio. The values of R_{Ni} for the numerous recorded PES data are included in Figure 2a.

The valence region is the result of the Ni 3d$^8\underline{Z}$ and the Ni 3d$^8\underline{L}$ final states near the photoemission extinction, and to higher binding energy, of the photoemission from the Ni 3d^7 orbital (see Figure 1c).[37] We evaluated the valence band maximum (E_{VBM}) by linear intersection of the extinction edge with the bandgap (see Figure 1f). Although the valence spectra are not totally equal to zero at the determined E_{VBM} value, this method is adopted for comparability reason with other studies.[39−41] Figure 1f shows that E_{VBM} shifts from ∼1.1 to ∼0.6 eV with increasing O 1s(Def.) weight. The shift to lower binding energy with increasing O 1s(Def.) weight is also observed in the Ni 2p and the O 1s region. For O 1s(def.) weight ≥10%, the Fermi level position is relatively constant.

To compare the numerous in situ X-ray and in situ ultraviolet PES measurements performed along this study, we have plotted in Figure 2a the parameters E_{VBM}, R_{Ni}, and the work function (ϕ) derived from the second electron emission cutoff (see Figure 2b) as well as the ionization potential $I = E_{\mathrm{VBM}} + \phi$[42] as a function of the weight of the O 1s(Def.) feature in the O 1s region. Figure 2c provides complementary optical measurements of RT- and HT-NiO thin films.

From Figure 2a, two domains can be identified based on the evolution of E_{VBM} and R_{Ni}. The first domain is composed by HT samples and is characterized by an O 1s(Def.) weight lower than 10% and a decreasing E_{VBM} with increasing O 1s(Def.) weight whereas R_{Ni} can be considered constant. The second domain, for O 1s (Def.) weight exceeding 10% and made of the samples prepared at room temperature, is characterized by a relatively constant E_{VBM} (∼0.6 eV) while a clear trend between R_{Ni} and the O 1s(Def.) weight is evident.

The evolution of R_{Ni} in the second domain can be associated with the formation of Ni^{3+} as this corresponds to the buildup of an extra electronic state in the Ni 2p region for such samples

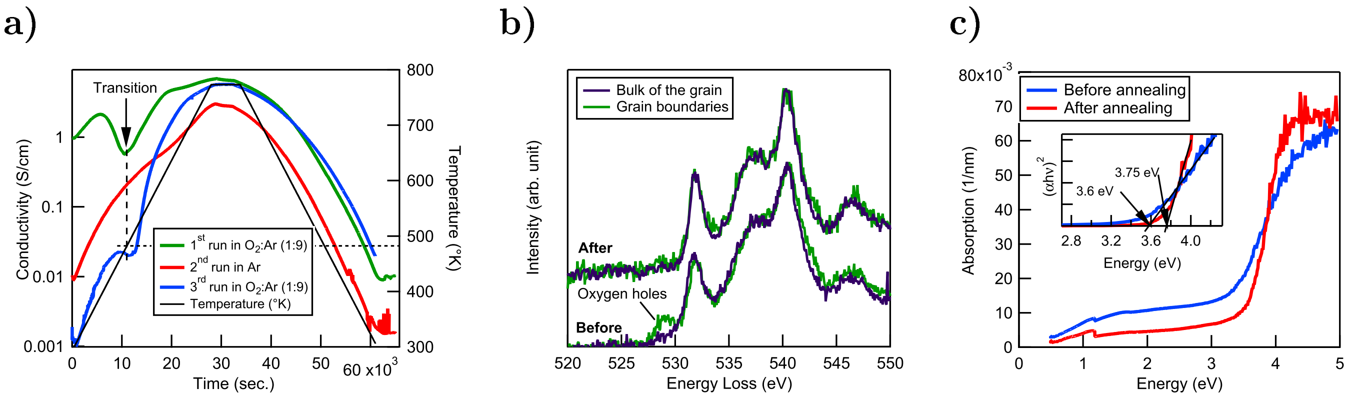

Figure 4. (a) Conductivity−temperature dependence of RT-NiO thin films prepared on fused silica with 15% oxygen in the deposition chamber. The temperature profile is indicated by the black curve. (b) EELS spectra obtained in the bulk of the grain and at the grain boundaries of the RT-NiO thin film on fused silica before and after annealing. (c) Optical measurements performed on an as-prepared film and an annealed RT-NiO thin film.

(see Figure 1d). In the absence of this extra electronic state associated with Ni^{3+}, the R_{Ni} ratio stands at around 0.625 for all the produced samples as observed in the first domain. Both domains are similarly influenced by the oxygen concentration during the deposition, i.e., the highest concentration of oxygen during the deposition results in the largest O 1s(Def.) weight in the O 1s region. A strong temperature dependence of the work function can be also noticed, which increases from ∼4.5 to ∼5.2 eV when the deposition temperature varies from 400 °C to room temperature. The higher work function measured on the RT-NiO thin films can be symptomatic of an accumulation of oxygen at the surface either because of the presence of peroxo species (O^-) on the NiO surface[43] or because of the increase of the cation electronegativity with higher oxidation state (e.g., $Ni^{2+} \rightarrow Ni^{3+}$).[7] It is commonly accepted that more oxidized surfaces exhibit a higher work function as oxygen would increase the surface ionization potential.[42] Thus, RT-NiO thin film surfaces are likely more oxidized than the HT thin film, and it results in the formation of a surface dipole δ of about 0.3 eV (see Figure 2d).

Interestingly, the optical measurements in Figure 2c show an increasing adsorption within the optical bandgap of the RT-NiO thin films when the oxygen concentration increases. This trend is not as much pronounced for the HT-NiO thin films. The strong adsorption at RT can originate from the higher defect concentration of these thin films. It is worth mentioning that comparable optical experiments performed on HT single crystalline Li-doped NiO thin films also report the presence of an acceptor state about 1 eV above the valence band, which introduces two optical transitions within the bandgap labeled α and β in Figure 2c.[40] No optical double features can be noticed for RT-NiO thin films in which the adsorption inside the bandgap is relatively monotonous. We suggest that in the case of the HT single crystal Li-doped NiO thin films the acceptor state has a sharp Ni 3d nature, but, as it will be detailed later, because of large disordered grain boundary regions rich in oxygen, the acceptor state might have an O 2p nature leading to a broad adsorption feature within the bandgap for RT-NiO thin films.

Finally, from this first batch of results, two NiO thin films categories can be identified according to the temperature of deposition. The RT-NiO thin films are characterized by a pinned Fermi level to about 0.6 eV, a high work function of about 5.2 eV, a high O 1s(Def.) weight, the presence of Ni^{3+}, and a lower optical transparency. On the contrary, HT-NiO thin films are characterized by an unpinned Fermi level, a lower work function of about 4.5 eV, a low O 1s(Def.) weight, the absence of Ni^{3+}, and a higher transparency. An energy diagram summary of both materials is represented in Figure 2d. In the following section, additional insights into the RT-NiO thin films properties are reported.

Additional Properties of RT-NiO Thin Films. RT-NiO thin films, characterized by a Fermi level pinning (see the second domain in Figure 2a), have been investigated by in situ electrical, STEM-EELS, and temperature-dependent electrical measurements.

As represented in Figure 3a, the in situ electrical measurements are performed on gold patterned fused silica substrate in a two-terminal configuration. The surface properties are also systematically measured by in situ X-ray PES without breaking the vacuum. In situ conductivity (Figure 3b) and the valence band maximum position to the Fermi level (Figure 3c) can be compared on the same material. In Figure 3a, the linear extrapolation of the total resistance (R_{tot}) as a function of the inverse of the thin film thickness $1/t$ enables one to remove the contribution of the contact resistance (R_c) and to estimate the thin film resistivity (ρ.cm) (i.e., the conductivity). The in situ electrical conductivity increases from $\sim 10^{-2}$ to $\sim 10^{1}$ S cm^{-1} with increasing oxygen concentration in the deposition chamber, whereas the Fermi level is unchanged with $E_{\mathrm{VBM}} \sim$ 0.6 eV, in agreement with what is observed for the RT-NiO thin films in Figure 2a. The measured electrical conductivity range is similar to numbers available in the literature for RT-NiO thin films.[21−23] This highlights that the RT-NiO thin films conductivity increases with the oxygen concentration whereas E_{VBM} remains constant.

Concurrently, the STEM-EELS measurements evidence the presence of a prepeak at 529 eV in the O K edge spectra which is more pronounced at the grain boundaries and can be detected inside the grain for high oxygen concentration (Figure 3c−e). The bicolor images (Figure 3e) derived from the STEM-EELS measurements also show that the chemical heterogeneity increases with increasing oxygen content in the deposition chamber. The prepeak has also been reported in both intrinsically and extrinsically doped NiO materials[30,40,44] and at point defects in an ordered NiO crystallographic structure.[45] As the presence and the intensity of the prepeak correlates with the conductivity of the NiO thin films, our

https://doi.org/10.1021/acsaelm.2c00230

results strongly suggest that the grain boundaries are more conductive than the bulk of the grains under oxygen-rich growth conditions at RT. Although the exact nature of the prepeak is controversial, its presence can be associated with positive charges in NiO[22,30,40,44,46] in the form of a hole in the Ni $3d^8\underline{L}$ state.[47] For this reason, this feature will be referred as an *oxygen hole* in the rest of this article.

The electrical conductivity of RT-NiO thin films has been further analyzed in a controlled atmosphere (Ar and O_2) by thermal cycling from RT to 500 °C (see Figure 4a). STEM-EELS measurements have been performed before and after the annealing. Before the experiment, the RT-NiO thin film displays a high electrical conductivity with 1 S/cm and an oxygen hole prepeak at 529 eV in the O−K edge spectra detected primarily at the grain boundaries. During the first thermal cycle, the conductivity undergoes a nonreversible transition at 150−200 °C when cycled with 10% oxygen in the atmosphere (Figure 4a). After this first cycle, the electrical conductivity at room temperature decreased by 2 orders of magnitude and does not return to the initial value. This result is in line with the literature, where it has been reported that the conductivity of NiO thin films abruptly losses up to 3 orders of magnitude when the NiO thin film is prepared above 200 °C in comparison to NiO thin films prepared at RT.[21] Interestingly, the conductivity of the NiO thin film can be affected by the presence of oxygen in the atmosphere during the thermal cycle. As observed in Figure 4a, at the end of the second cycle, performed in pure argon, the conductivity is decreased by another order of magnitude in comparison to its value at the end of the first cycle, which has been performed in a 10% O_2 atmosphere. On the contrary, the final conductivity value after the third cycle, again executed with 10% oxygen, is identical with the conductivity obtained at the end of the first cycle (Figure 4a). Interestingly, the epitaxial NiO thin films produced at HT, regardless of the orientation, are not as much sensitive to oxygen and presents a lower conductivity in comparison to the polycrystalline thin films upon thermal cycling (see Figure S6). This can demonstrate that grain boundaries facilitate p-doping because of an enhanced oxygen diffusion in polycrystalline NiO thin films.

After the thermal cycles, when characterized by EELS, the thin film does not display any oxygen hole prepeak at 529 eV in the O−K edge region, not even at the grain boundaries (Figure 4b), whereas the thin film structure is well preserved with columnar grains parallel to the direction of growth, as observed before annealing (see Figure S2). Evidently, the thermal cycle suppresses the defects formed at the grain boundaries during deposition at room temperature while preserving the microstructure of the film. It is suggested that the annealing step relaxes and converts the RT-NiO thin film toward a more stoichiometric and homogeneous composition and more ordered structure, particularly at the grain boundaries. As the RT-NiO thin films are oxygen-rich, particularly by the formation of an oxygen-rich secondary phase at the grain boundaries, it can be assumed that heating above 200 °C enables to restore stoichiometry homogeneity in the thin films. This can be associated with the desorption of the excess of oxygen present at the grain boundaries upon heating.

Optical measurement shows that the nonannealed sample prepared at room temperature has a higher optical absorption in the bandgap in comparison to the annealed sample (Figure 4c). In the meantime, although this might be not substantial, the optical bandgap increases from 3.6 to 3.75 eV (Figure 4c). The higher optical absorption observed for the sample prepared at RT is suggested to be related to the oxygen hole species evidenced by STEM-EELS measurements. Indeed, for the annealed sample, the absorption in the bandgap is substantially reduced while the oxygen hole prepeak is removed (Figure 4b).

The experiments performed on RT-NiO thin films highlight the electrical properties and the chemical heterogeneity of such films. In particular, although the Fermi level position is unchanged, higher thin film conductivity is obtained with higher oxygen pressure during deposition. Concurrently, a temperature unstable secondary phase rich in oxygen holes accumulates at the grain boundaries. In the coming section, a unifying charge compensation of intrinsic defects in RT- and HT-NiO thin films is discussed on the basis of results reported above.

DISCUSSION

It is generally accepted that p-type conductivity in a perfect NiO crystallographic structure can be obtained by metallic deficiency ($Ni_{1-x}O$) in the form of nickel vacancies V''_{Ni}.[3,27−30] However, as shown in Figure 3, the RT-NiO thin films contain grain boundaries full with oxygen holes and can likely provide support for higher electrical conductivity. Thus, the acceptor concentration must be enriched at the grain boundaries. It is suggested that both nickel vacancies (V''_{Ni}) and oxygen interstitials (O''_i) can participate in p-doping of RT-NiO thin films. It is noted that NiO room temperature films can contain metastable defect configuration due to low diffusion coefficients. In this prospect, we assume that the highest binding energy O 1s(Def.) component for RT-NiO thin films in Figure 1e actually originates from the oxygen interstitial while the lowest from peroxo species ($O^\bullet_o$) or surface oxygen (O_S).

For charge neutrality, the negatively charged intrinsic acceptors V_{Ni}'' and O_i'' have to be compensated by positive charges such as free (delocalized) holes ($h^\bullet$) or by localized holes either on oxygen and or on nickel atoms. The latter corresponds to peroxo species O^- ($O^\bullet_o$) or Ni^{3+} ($Ni^\bullet_{Ni}$), respectively.[30] In addition, it should be mentioned that in an oxygen-rich environment the formation of oxygen vacancies is not expected and thus is neglected. Therefore, the charge neutrality condition in NiO thin films can be written as

$$2[V''_{Ni}] + 2[O''_i] = [h^\bullet] + [Ni^\bullet_{Ni}] + [O^\bullet_O] \tag{2}$$

where the brackets "[ ]" correspond to the volumetric concentrations of the species. The left-hand side of eq 2 is the intrinsic acceptors, which generate charges in NiO thin films, while the right-hand side represents the charge-compensating species of the dopants.

Taking the right-hand side of eq 2, the conductivity (σ) in NiO thin films originates from the contribution of free and trapped charges and can be expressed as follows:

$$\sigma = q([h^\bullet]\mu_{h^\bullet} + [Ni^\bullet_{Ni}]\mu_{Ni^\bullet_{Ni}} + [O^\bullet_O]\mu_{O^\bullet_O}) \tag{3}$$

with q the elementary charge and μ the mobility. According to Fermi statistics, the concentration of free holes $[h^\bullet]$ in the valence band is

$$[h^\bullet] = N_v \exp\left(-\frac{E_F - E_{VBM}}{k_B T}\right) \tag{4}$$

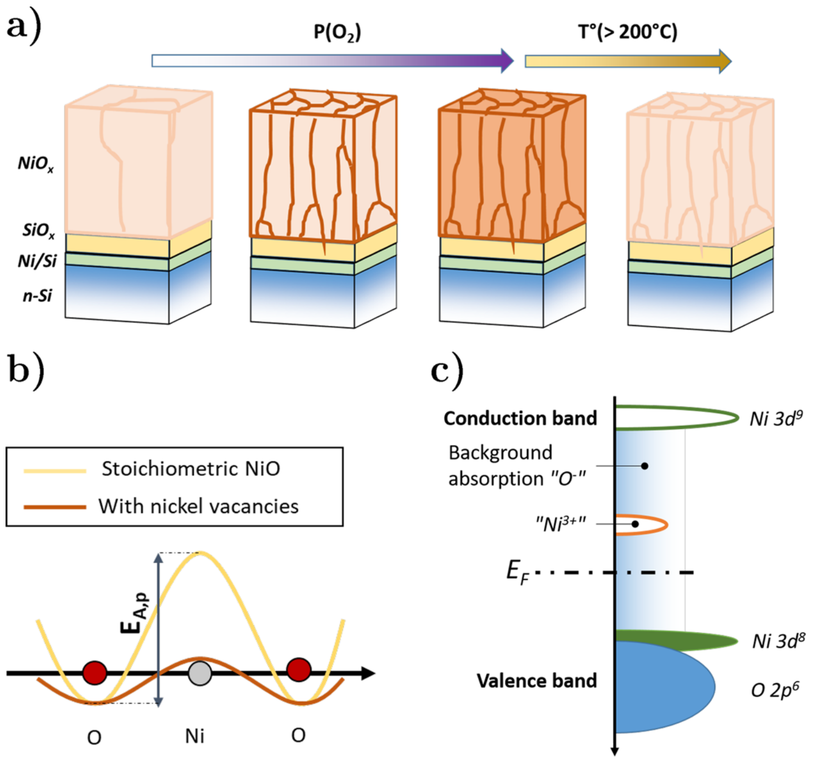

Figure 5. (a) Representation of the distribution of the oxygen holes throughout the 50 nm RT-NiO thin films deposited on the oxide-free silicon surface according to the oxygen partial pressure in the deposition chamber as deduced from Figure 3. The darker red colors indicate a higher oxygen concentration. As detailed in Figure S4, cationic interdiffusion occurs at the interface which leads to the formation of a SiO_x layer on top of a nickel rich region. High conductivity in RT-NiO thin films could originate from (b) a reduction of the potential profile encountered by a charge during a polaron hopping process in an oxygen-rich material (reduced energy wall $E_{A,p}$) in comparison to a stoichiometric NiO structure (high-energy wall $E_{A,p}$) or (c) the presence of additional energy level in the NiO bandgap associated with positively trapped species which can participate in the electrical conduction process.

with N_v the effective density of states in the valence band, E_F the Fermi energy, E_{VBM} the valence band maximum, T the temperature, and k_B the Boltzmann constant.

Because of the anticipated low mobility of the trapped holes, it is suggested that the increase of the conductivity of RT-NiO with increasing oxygen activity is related only to the concentration $[h^\bullet]$ in the valence band; eq 4 can be written in the form

$$E_{F,15\%} - E_{F,5\%} = -k_B T \ln\left(\frac{[h^\bullet]_{15\%}}{[h^\bullet]_{5\%}}\right) \tag{5}$$

In Figure 3, it is shown that the conductivity increases by 3 orders of magnitude when the oxygen concentration increases from 5% to 15% during the deposition. If this conductivity increase is solely caused by an increase in the concentration of free holes, according to eq 5, a decrease of the binding energy of the valence band maximum, the Ni $3d^8$, and the O 1s peaks by about 0.2 eV should be observed. This is experimentally not observed as seen in Figures 3c and in Figure 2 where the surface Fermi energy is pinned at 0.6 eV above the valence band maximum for any RT-NiO films. The observed surface Fermi level pinning at 0.6 eV by PES for RT-NiO thin films can produce a depletion zone in the surface vicinity of the thin films due to electron trapping by surface defects. In addition, the EELS measurements show that the defects are detected first at the grain boundaries before entering the bulk of the grain with increasing oxygen-rich conditions of preparation (Figure 3f). The defect concentration must be at least >1% as they are detected both by PES and EELS measurements. For such concentration, the width of the depletion layer at the grain boundaries must be in the nanometers range for a defect-free bulk.[48−51] It can be, however, assumed that ionic oxygen bombardment under reactive sputtering[9] induces defects that are immobilized at room temperature in the thin films structure, even when sputtered at low oxygen concentration. Therefore, bulk defects cannot be excluded at room temperature although not detected by EELS. Thus, the surface Fermi level pinning can be also an indication of bulk Fermi level pinning for such thin films. With regard to the HT-NiO thin films of the first domain in Figure 2a and as indicated by our previous study,[31] the bulk Fermi energy might be higher than the surface Fermi energy, but it cannot be closer to the valence band maximum than the limit observed at the surface and it cannot be larger than the 1 eV limit observed for defect free surfaces (Figure 2a).

As a consequence, the charge compensation cannot be realized by free holes $(h^\bullet)$ inside the grains for the RT-NiO thin films. This Fermi level pinning could be the result of the presence of a deep acceptor level with a charge transition at 0.6 eV above the valence band[27] and to the formation of a bound polaron (localized holes)[41] in the vicinity of a nickel vacancy for RT-NiO thin films. This Fermi level pinning does not seem to be present for Li-doped NiO where experimental and theoretical studies suggest that the Fermi level can be close to the valence band edge upon Li doping.[27,40]

In addition, Figure 2 shows that for RT-NiO thin films the R_{Ni} increases with the increase of the O 1s(Def.) weight. We assume that the additional feature in the Ni 2p region near the peak satellite can be associated with the formation of trapped charges on nickel leading to Ni^{3+} while the lower binding energy component of the O 1s(Def.) originates from the formation of localized trapped charges on oxygen leading to the formation of peroxo species (O^-). Therefore, we propose that dopants in RT-NiO thin films are not electronically compensated by free holes but rather by localized positive charges on the oxygen and the nickel atoms.

$$2[V_{Ni}''] + 2[O_i''] = [Ni_{Ni}^{\bullet}] + [O_O^{\bullet}] \tag{6}$$

In spite of bulk Fermi level pinning, the RT-NiO thin films display higher conductivity with increasing oxygen concentration. Concurrently, oxygen holes, which can be associated with a fingerprint of an higher conductivity, are measured primarily at the grain boundaries, and they are more significant with increasing oxygen partial pressure (Figure 3d,e and scheme in Figure 5a). Therefore, it can be assumed that the grain boundaries can be the main path for the electrical conductivity and that they are oxygen-rich. According to the analysis of the grain boundaries distribution (see Figures S2 and S3), the density of grain boundaries does not substantially increases with increasing oxygen concentration for RT-NiO thin films in the thickness range of the samples produced in this study. Therefore, the increase of the in situ conductivity in Figure 3b is likely related to a change in the grain boundaries chemistry which can present higher defects concentration in more oxygen-rich conditions. However, Keraudy et al. reported that for a given grain boundaries chemistry the conductivity of the thin films decreased with decreasing grain boundaries density for thin films thickness range of 100−1000 nm.[25] This result supports the assumption that the grain boundaries promote the electrical conductivity in the NiO thin films. Eventually, the conductivity at the grain boundaries can be estimated from a brick layer model.[52] We find that the grain boundary conductivity σ_{GB} can be as high as 4 S/cm while the bulk of the grain is in 10^{-2} S/cm range (see the calculation in Supporting Information section S2.2). These values indicate that grain boundaries can be up to 400 times more conductive than the bulk of the grain. The determination of the carrier concentration or the charge mobility in nonintentionally doped NiO thin films is quite difficult because of the electrical hopping transport in such materials. To the best of our knowledge, literature does not provide reliable quantitative insights but to explain the reported high electrical conductivity and the low electrical activation energy for RT-NiO thin films in comparison to nondoped NiO structures (see the Introduction), we propose two underlying charge transport mechanisms based on qualitative considerations. A combination of both mechanisms is not excluded.

As a first mechanism, we propose that the high conductivity could originate from the formation of a O 2p continuous band at the grain boundaries replacing the charge-transfer mechanism in standard NiO. The continuous band at the grain boundaries would drastically reduce the electrical activation energy necessary for the charge displacement relying on polaron hopping (see Figure 5b) while the bulk of the grain would be still subjected to large charge-transfer resistivity.[36,38,53] Such case would necessarily lead to a considerable increase of the charge mobility at the grain boundaries.

The second mechanism could arise as a consequence of the Fermi level pinning due to charge compensation of dopants in the form of trapped charges such as O^- and Ni^{3+}. Similarly to Li-doped and oxygen-deficient NiO materials,[54,55] we assume that these trapped charges in RT-NiO thin films are localized at intermediate energy levels in the NiO bandgap, and so, if they are mobile, they do not circulate in the valence band but in another energy level (Figure 5c). This additional energy level can bring another electrical path participating in the overall conductivity as described in eq 3.

As represented in Figure 5a, the oxygen-rich grain boundaries are eliminated by annealing. It implies that the oxygen-rich phase is not stable. This instability can be also the underlying mechanism leading to electrical aging and to the higher chemical reactivity of RT-NiO thin films.[23,56,57] After annealing, the grain boundaries and the bulk of the grains are more homogeneous, no oxygen-holes are detected, and in situ X-ray PES does not evidence the presence of oxygen interstitials for HT-NiO thin films. Therefore, we assume that only nickel vacancies (V_{Ni}'') can compensate for the stoichiometry deviation in HT-NiO thin films. Meanwhile, the Ni 2p region is not particularly affected by the increase of the O 1s(Def.) weight for HT-NiO thin films as evidenced by the constant R_{Ni} ratio (see Figure 2a). It would mean that the defects produced at high temperature are not charge compensated by Ni^{3+}, but it still can be conceived they are compensated by positive charges on the oxygen atoms. Indeed, as charge transfer material where mobile charges periodically hop from an anionic to a cationic site, it is quite realistic that nickel vacancies in an otherwise perfect NiO structure are electronically compensated by an electrical distribution on the closest neighboring atoms.[53] The concentration of these positive charges on oxygen which would lead to peroxo species is too low for being detected by the PES and STEM-EELS setup. Thus, the O 1s(Def.) feature for HT-NiO thin films in Figure 1b,e could instead originate from adsorbed oxygen on the thin films surface for which the concentration could be proportional to the defectiveness of the NiO thin films. In any case, the decreasing valence band edge position to the Fermi level with increasing O 1s(Def.) weight (see Figure 2) can be interpreted as an increase of the free holes concentration in the valence band (see Figure 4) for HT-NiO thin films with increasing defects (nickel vacancies) concentration. Finally, we propose that for the NiO thin films produced at high temperature, visible in the first domain in Figure 2, the compensation of nickel vacancies is realized by the formation of free holes and peroxo species:

$$2[V_{Ni}''] = [h^{\bullet}] + [O_O^{\bullet}] \tag{7}$$

■ CONCLUSION

This study evidences that polycrystalline reactively sputtered NiO thin films can have drastic different properties at electronic, chemical, and defect levels when prepared either at RT or at HT. Thus, HT-NiO thin films display a low work function (∼4.5 eV), an unpinned Fermi level (0.6−1.1 eV), high transparency, poor electrical conductivity, and good stoichiometric homogeneity. On the contrary, RT-NiO thin films show a high work function (∼5.2 eV), Fermi level pinning (∼0.6 eV), lower transparency, high electrical conductivity, a surface dipole of 0.3 eV, and a high stoichiometric heterogeneity with the appearance of an oxygen-rich phase at the thin film grain boundaries with increasing oxygen concentration. In addition, the HT-NiO thin films are doped by nickel vacancies which are charge compensated by free holes and localized holes on the surrounding oxygen atoms, but in RT-NiO thin films the dopants can be both nickel vacancies and oxygen interstitials which are charge compensated solely by localized holes on both nickel and oxygen atoms. The high electrical conductivity of RT-NiO thin films originates from the highly conductive grain boundaries because of a lowering of the electrical activation barrier or because of a different electrical transportation mechanism through trapped charges. The defects at and the conduction along the grain boundaries in RT-NiO thin films can be suppressed with an annealing step above 200 °C.

■ ASSOCIATED CONTENT

Supporting Information

The Supporting Information is available free of charge at https://pubs.acs.org/doi/10.1021/acsaelm.2c00230.

> Experiments with the preparation of thin films and their characterization by photoelectron spectroscopy (PES), conductivity−temperature dependence experiment, scanning transmission electron microscopy coupled with electron energy loss spectroscopy (STEM-EELS), automated crystal orientation mapping (ACOM-TEM), and optical measurements; additional results including thin film crystallographic microstructure, grain conductivity calculation, chemical transition between silicon with sputtered NiO thin films, and cross-section images of epitaxial NiO thin films on the oriented MgO monocrystal (PDF)

■ AUTHOR INFORMATION

Corresponding Author

Andreas Klein − *Institute of Materials Science, Electronic Structure of Materials, Technical University of Darmstadt, 64287 Darmstadt, Germany;* orcid.org/0000-0001-7463-1495; Email: aklein@esm.tu-darmstadt.de

Authors

Raphaël Poulain − *Institute of Materials Science, Electronic Structure of Materials, Technical University of Darmstadt, 64287 Darmstadt, Germany; Materials and Process Engineering, Université Catholique de Louvain, 1348 Louvain-La-Neuve, Belgium;* orcid.org/0000-0003-3813-9668

Gunnar Lumbeeck − *Electron Microscopy for Materials Science, University of Antwerp, 2020 Antwerpen, Belgium*

Jonas Hunka − *Institute of Materials Science, Electronic Structure of Materials, Technical University of Darmstadt, 64287 Darmstadt, Germany*

Joris Proost − *Materials and Process Engineering, Université Catholique de Louvain, 1348 Louvain-La-Neuve, Belgium;* orcid.org/0000-0003-2220-1893

Henri Savolainen − *Institute of Materials Science, Electronic Structure of Materials, Technical University of Darmstadt, 64287 Darmstadt, Germany*

Hosni Idrissi − *Materials and Process Engineering, Université Catholique de Louvain, 1348 Louvain-La-Neuve, Belgium; Electron Microscopy for Materials Science, University of Antwerp, 2020 Antwerpen, Belgium*

Dominique Schryvers − *Electron Microscopy for Materials Science, University of Antwerp, 2020 Antwerpen, Belgium*

Nicolas Gauquelin − *Electron Microscopy for Materials Science, University of Antwerp, 2020 Antwerpen, Belgium*

Complete contact information is available at: https://pubs.acs.org/10.1021/acsaelm.2c00230

Author Contributions

R.P. and J.H. prepared the thin films and performed in situ XPS and in situ electrical measurements, H.S. realized the conductivity−temperature dependence measurements, and G.L., N.G., D.S., and H.I. performed and analyzed the TEM measurements. R.P., J.P., G.L., A.K., and N.G. conceived the research, designed the experiments, and drafted the manuscript. All the authors discussed the results and participated in writing the manuscript.

Notes

The authors declare no competing financial interest.

■ ACKNOWLEDGMENTS

This work was funded by the European Union's Horizon 2020 Research and Innovation Programme under the Marie Sklodowska-Curie Grant Agreement No. 641640 (EJD-ITN project FunMAT). It was also supported by the Hercules Foundation [Grant No. AUHA13009] and the Flemish Research Fund (FWO) [Grant No. G.0365.15N]. H. Idrissi is mandated by the Belgian National Fund for Scientific Research (FSR-FNRS). The authors also cordially thank the technical team of the Wallonia Infrastructure for Nano FABrication (Winfab) platform.

■ REFERENCES

(1) Lunkenheimer, P.; Loidl, A.; Ottermann, C. R.; Bange, K. Correlated barrier hopping in NiO films. *Phys. Rev. B* **1991**, *44*, 5927−5930.

(2) Adler, D.; Feinleib, J. Electrical and Optical Properties of Narrow-Band Materials. *Phys. Rev. B* **1970**, *2*, 3112−3134.

(3) Jiang, F.; Choy, W. C. H.; Li, X.; Zhang, D.; Cheng, J. Post-treatment-Free Solution-Processed Non-stoichiometric NiOx Nanoparticles for Efficient Hole-Transport Layers of Organic Optoelectronic Devices. *Adv. Mater.* **2015**, *27*, 2930−2937.

(4) Nayak, M.; Mandal, S.; Pandey, A.; Mudgal, S.; Singh, S.; Komarala, V. K. Nickel Oxide Hole-Selective Heterocontact for Silicon Solar Cells: Role of SiOx Interlayer on Device Performance. *Solar RRL* **2019**, *3*, 1900261.

(5) Greiner, M. T.; Helander, M. G.; Tang, W.-M.; Wang, Z.-B.; Qiu, J.; Lu, Z.-H. Universal energy-level alignment of molecules on metal oxides. *Nat. Mater.* **2012**, *11*, 76−81.

(6) Greiner, M. T.; Helander, M. G.; Wang, Z. B.; Tang, W. M.; Lu, Z. H. Effects of Processing Conditions on the Work Function and Energy-Level Alignment of NiO Thin Films. *J. Phys. Chem. C* **2010**, *114*, 19777−19781.

(7) Greiner, M. T.; Chai, L.; Helander, M. G.; Tang, W. M.; Lu, Z. H. Transition Metal Oxide Work Functions: The Influence of Cation Oxidation State and Oxygen Vacancies. *Adv. Funct. Mater.* **2012**, *22*, 4557−4568.

(8) Tengeler, S.; Fingerle, M.; Calvet, W.; Steinert, C.; Kaiser, B.; Mayer, T.; Jaegermann, W. The Impact of Different Si Surface Terminations in the (001) n-Si/NiO$_x$ Heterojunction on the Oxygen Evolution Reaction (OER) by XPS and Electrochemical Methods. *J. Electrochem. Soc.* **2018**, *165*, 3122−3130.

(9) Poulain, R.; Proost, J.; Klein, A. Sputter Deposition of Transition Metal Oxides on Silicon: Evidencing the Role of Oxygen Bombardment for Fermi-Level Pinning. *phys. status solidi (a)* **2019**, *216*, 1900730.

(10) Waser, R.; Dittmann, R.; Salinga, M.; Wuttig, M. Function by defects at the atomic scale - New concepts for non-volatile memories. *Solid-State Electron.* **2010**, *54*, 830−840.

(11) Lee, M.-J.; Park, Y.; Suh, D.-S.; Lee, E.-H.; Seo, S.; Kim, D.-C.; Jung, R.; Kang, B.-S.; Ahn, S.-E.; Lee, C.; Seo, D.; Cha, Y.-K.; Yoo, I.-K.; Kim, J.-S.; Park, B. Two Series Oxide Resistors Applicable to High

Speed and High Density Nonvolatile Memory. *Adv. Mater.* **2007**, *19*, 3919−3923.

(12) Mokoena, T. P.; Swart, H. C.; Motaung, D. E. A review on recent progress of p-type nickel oxide based gas sensors: Future perspectives. *J. Alloys Compd.* **2019**, *805*, 267−294.

(13) Miller, E. L.; Rocheleau, R. E. Electrochemical and electrochromic behavior of reactively sputtered nickel oxide. *J. Electrochem. Soc.* **1997**, *144*, 1995−2003.

(14) Huang, J.; Sun, Y.; Du, X.; Zhang, Y.; Wu, C.; Yan, C.; Yan, Y.; Zou, G.; Wu, W.; Lu, R.; Li, Y.; Xiong, J. Cytomembrane-Structure-Inspired Active Ni-N-O Interface for Enhanced Oxygen Evolution Reaction. *Adv. Mater.* **2018**, *30*, 1803367.

(15) Liu, Y.; Gao, C.; Li, Q.; Pang, H. Nickel Oxide/Graphene Composites: Synthesis and Applications. *Chem.—Eur. J.* **2019**, *25*, 2141−2160.

(16) Poulain, R.; Klein, A.; Proost, J. Electrocatalytic Properties of (100)-, (110)-, and (111)-Oriented NiO Thin Films toward the Oxygen Evolution Reaction. *J. Phys. Chem. C* **2018**, *122*, 22252−22263.

(17) Mei, J.; Liao, T.; Kou, L.; Sun, Z. Two-Dimensional Metal Oxide Nanomaterials for Next-Generation Rechargeable Batteries. *Adv. Mater.* **2017**, *29*, 1700176.

(18) Shao, J.-J.; Lv, W.; Yang, Q.-H. Self-Assembly of Graphene Oxide at Interfaces. *Adv. Mater.* **2014**, *26*, 5586−5612.

(19) Li, W.; Erickson, E. M.; Manthiram, A. High-nickel layered oxide cathodes for lithium-based automotive batteries. *Nat. Energy* **2020**, *5*, 26−34.

(20) Patil, R. A.; Devan, R. S.; Lin, J.-H.; Liou, Y.; Ma, Y.-R. An efficient methodology for measurement of the average electrical properties of single one-dimensional NiO nanorods. *Sci. Rep.* **2013**, *3*, 3070.

(21) Sato, H.; Minami, T.; Takata, S.; Yamada, T. Transparent Conducting p-Type NiO Thin-Films Prepared by Magnetron Sputtering. *Thin Solid Films* **1993**, *236*, 27−31.

(22) Mossanek, R. J.; Dominguez-Canizares, G.; Gutierrez, A.; Abbate, M.; Diaz-Fernandez, D.; Soriano, L. Effects of Ni vacancies and crystallite size on the O 1s and Ni 2p X-ray absorption spectra of nanocrystalline NiO. *J. Phys.: Condens. Matter* **2013**, *25*, 495506.

(23) Chen, H.-L.; Lu, Y.-M.; Hwang, W.-S. Characterization of sputtered NiO thin films. *Surf. Coat. Technol.* **2005**, *198*, 138−142.

(24) Hakim, A.; Hossain, J.; Khan, K. A. Temperature effect on the electrical properties of undoped NiO thin films. *Renew. Energy* **2009**, *34*, 2625−2629.

(25) Keraudy, J.; Molleja, J. G.; Ferrec, A.; Corraze, B.; Richard-Plouet, M.; Goullet, A.; Jouan, P. Y. Structural, morphological and electrical properties of nickel oxide thin films deposited by reactive sputtering. *Appl. Surf. Sci.* **2015**, *357*, 838−844.

(26) Reissner, R.; Schulze, M. Multilayer adsorption of water on NiO(100) at 120 and 143 K. *Surf. Sci.* **2000**, *454*, 183−190.

(27) Lany, S.; Osorio-Guillen, J.; Zunger, A. Origins of the doping asymmetry in oxides: Hole doping in NiO versus electron doping in ZnO. *Phys. Rev. B* **2007**, *75*, 241203.

(28) Park, S.; Ahn, H.-S.; Lee, C.-K.; Kim, H.; Jin, H.; Lee, H.-S.; Seo, S.; Yu, J.; Han, S. Interaction and ordering of vacancy defects in NiO. *Phys. Rev. B* **2008**, *77*, 134103.

(29) Zhang, J.; Zeng, D.; Zhu, Q.; Wu, J.; Huang, Q.; Xie, C. Effect of Nickel Vacancies on the Room-Temperature NO_2 Sensing Properties of Mesoporous NiO Nanosheets. *J. Phys. Chem. C* **2016**, *120*, 3936−3945.

(30) Cho, D. Y.; Song, S. J.; Kim, U. K.; Kim, K. M.; Lee, H. K.; Hwang, C. S. Spectroscopic investigation of the hole states in Ni-deficient NiO films. *J. Mater. Chem. C* **2013**, *1*, 4334−4338.

(31) Poulain, R.; Rohrer, J.; Hermans, Y.; Dietz, C.; Brötz, J.; Proost, J.; Chatenet, M.; Klein, A. Origin of Surface Reduction upon Water Adsorption on Oriented NiO Thin Films and Its Relation to Electrochemical Activity. *J. Phys. Chem. C* **2022**, *126*, 1303−1315.

(32) Dupin, J.-C.; Gonbeau, D.; Vinatier, P.; Levasseur, A. Systematic XPS studies of metal oxides, hydroxides and peroxides. *Phys. Chem. Chem. Phys.* **2000**, *2*, 1319−1324.

(33) Hufner, S. Electronic-Structure of NiO and Related 3d-Transition-Metal Compounds. *Adv. Phys.* **1994**, *43*, 183−356.

(34) Bagus, P. S.; Broer, R.; de Graaf, C.; Nieuwpoort, W. C. The electronic structure of NiO for Ni 3s-hole states including full orbital relaxation and localization. *J. Electron. Spectroscp.* **1999**, *98*, 303−319.

(35) Kuo, C. Y.; Haupricht, T.; Weinen, J.; Wu, H.; Tsuei, K. D.; Haverkort, M. W.; Tanaka, A.; Tjeng, L. H. Challenges from experiment: electronic structure of NiO. *Eur. Phys. J.-Spec. Top.* **2017**, *226*, 2445−2456.

(36) Lany, S. Semiconducting transition metal oxides. *J. Phys.: Condens. Matter* **2015**, *27*, 283203.

(37) Taguchi, M.; Matsunami, M.; Ishida, Y.; Eguchi, R.; Chainani, A.; Takata, Y.; Yabashi, M.; Tamasaku, K.; Nishino, Y.; Ishikawa, T.; Senba, Y.; Ohashi, H.; Shin, S. Revisiting the valence-band and core-level photoemission spectra of NiO. *Phys. Rev. Lett.* **2008**, *100*, 206401.

(38) Zaanen, J.; Sawatzky, G. A.; Allen, J. W. Band gaps and electronic structure of transition-metal compounds. *Phys. Rev. Lett.* **1985**, *55*, 418−421.

(39) Klein, A. Interface Properties of Dielectric Oxides. *J. Am. Ceram. Soc.* **2016**, *99*, 369−387.

(40) Zhang, J. Y.; Li, W. W.; Hoye, R. L. Z.; MacManus-Driscoll, J. L.; Budde, M.; Bierwagen, O.; Wang, L.; Du, Y.; Wahila, M. J.; Piper, L. F. J.; Lee, T. L.; Edwards, H. J.; Dhanak, V. R.; Zhang, K. H. L. Electronic and transport properties of Li-doped NiO epitaxial thin films. *J. Mater. Chem. C* **2018**, *6*, 2275−2282.

(41) Lohaus, C.; Klein, A.; Jaegermann, W. Limitation of Fermi level shifts by polaron defect states in hematite photoelectrodes. *Nat. Commun.* **2018**, *9*, 4309.

(42) Klein, A. Transparent Conducting Oxides: Electronic Structureroperty Relationship from Photoelectron Spectroscopy with in situ Sample Preparation. *J. Am. Ceram. Soc.* **2013**, *96*, 331−345.

(43) McKay, J. M.; Henrich, V. E. Surface electronic structure of NiO: Defect states, O_2 and H_2O interactions. *Phys. Rev. B* **1985**, *32*, 6764−6772.

(44) Kuiper, P.; Kruizinga, G.; Ghijsen, J.; Sawatzky, G. A.; Verweij, H. Character of holes in $Li_xNi_{1-x}O$ and their magnetic behavior. *Phys. Rev. Lett.* **1989**, *62*, 221−224.

(45) Sugiyama, I.; Shibata, N.; Wang, Z.; Kobayashi, S.; Yamamoto, T.; Ikuhara, Y. Ferromagnetic dislocations in antiferromagnetic NiO. *Nat. Nano.* **2013**, *8*, 266−270.

(46) Palina, N.; Wang, L.; Dash, S.; Yu, X.; Breese, M. B. H.; Wang, J.; Rusydi, A. Investigation of the metal-insulator transition in NdNiO3 films by site-selective X-ray absorption spectroscopy. *Nanoscale* **2017**, *9*, 6094−6102.

(47) Gauquelin, N.; Benckiser, E.; Kinyanjui, M. K.; Wu, M.; Lu, Y.; Christiani, G.; Logvenov, G.; Habermeier, H. U.; Kaiser, U.; Keimer, B.; Botton, G. A. Atomically resolved EELS mapping of the interfacial structure of epitaxially strained $LaNiO_3/LaAlO_3$ superlattices. *Phys. Rev. B* **2014**, *90*, 195140.

(48) Zurhelle, A. F.; Tong, X.; Klein, A.; Mebane, D. S.; DeSouza, R. A. A Space-Charge Treatment of the Increased Concentration of Reactive Species at the Surface of a Ceria Solid Solution. *Angew. Chem., Int. Ed.* **2017**, *56*, 14516−14520.

(49) Schuldt, K. N. S.; Ding, H.; Jaud, J.-C.; Koruza, J.; Klein, A. Influence of Defects on the Schottky Barrier Height at $BaTiO_3/RuO_2$ Interfaces. *phys. status solidi (a)* **2021**, *218*, 2100143.

(50) De Souza, R. A. Oxygen Diffusion in $SrTiO_3$ and Related Perovskite Oxides. *Adv. Funct. Mater.* **2015**, *25*, 6326−6342.

(51) Wardenga, H. F.; Schuldt, K. N. S.; Waldow, S.; De Souza, R. A.; Klein, A. Surface potentials of acceptor- and donor-doped CeO_2 thin films and their relation to oxygen surface exchange. *Phys. Chem. Chem. Phys.* **2022**, *24*, 1072−1080.

(52) Kidner, N. J.; Homrighaus, Z. J.; Ingram, B. J.; Mason, T. O.; Garboczi, E. Impedance/Dielectric Spectroscopy of Electroceramics—Part 1: Evaluation of Composite Models for Polycrystalline Ceramics. *J. Electroceram.* **2005**, *14*, 283−291.

(53) Castell, M.; Dudarev, S.; Wincott, P.; Condon, N.; Muggelberg, C.; Thornton, G.; Nguyen Manh, D.; Sutton, A.; Briggs, G. Atomic Resolution STM of the NiO (001) Surface Structure and Defect Sites: c(2 × 2) patterning and effects of covalent bonding. *Surf. Rev. Lett.* **1997**, *4*, 1003.

(54) Reinert, F.; Steiner, P.; et al. Electron and hole doping in NiO. *Z. Phys. B Cond. Mater.* **1995**, *97*, 83−93.

(55) van Elp, J.; Eskes, H.; Kuiper, P.; Sawatzky, G. A. Electronic structure of Li-doped NiO. *Phys. Rev. B* **1992**, *45*, 1612−1622.

(56) Jang, W. L.; Lu, Y. M.; Hwang, W. S.; Hsiung, T. L.; Wang, H. P. Effect of substrate temperature on the electrically conductive stability of sputtered NiO films. *Surf. Coat. Technol.* **2008**, *202*, 5444−5447.

(57) Jang, W.-L.; Lu, Y.-M.; Hwang, W.-S. Effect of different atmospheres on the electrical stabilization of NiO films. *Vac.* **2008**, *83*, 596−598.

https://doi.org/10.1021/acsaelm.2c00230
ACS Appl. Electron. Mater. 2022, 4, 2718−2728